JOURNAL OF COMPUTATIONAL PHYSICS 105, 306–323 (1993)

A Multidimensional Flux Function with Applications to the Euler and Navier–Stokes Equations

CHRISTOPHER L. RUMSEY

NASA Langley Research Center, Hampton, Virginia 23681

AND

BRAM VAN LEER AND PHILIP L. ROE

University of Michigan Ann Arbor, Michigan 48109

Received March 11, 1992; revised July 23, 1992

A grid-independent approximate Riemann solver has been developed for use in both two- and three-dimensional flows governed by the Euler or Navier–Stokes equations. Fluxes on grid faces are obtained via wave decomposition. By assuming that information propagates in the velocity-difference directions, rather than in the grid-normal directions as in a standard grid-aligned solver, this flux function more appropriately interprets and hence more accurately resolves shock and shear waves when these lie oblique to the grid. The model, which describes the difference in states at each grid interface by the action of five waves, produces a significant increase in accuracy for both supersonic and subsonic first-order spatially accurate computations. Second-order computations with the grid-independent flux function are generally only worth the additional effort for flowfields whose primary structures include shear waves that lie oblique to the grid. Included in this category is the viscous flow over an airfoil in which a separated shear layer emanates from the airfoil surface at an angle to the grid. Pressure distortions which can result from misinterpretation of the oblique waves by a grid-aligned solver are essentially eliminated by the grid-independent flux function.

INTRODUCTION

Among today's flow-solvers for the Euler and Navier–Stokes equations, many are based on upwind differencing. Prominent are Godunov-type schemes, in which the upwind bias is achieved by using the solution to the Riemann problem defined at each cell face. The Riemann problem can be solved exactly with an iterative method, as Godunov [3] did, or approximately, as Roe [11] did, leading to the concept of the "approximate Riemann solver." In Roe's method the Euler equations are linearized about an average state and then solved exactly. Different types of waves, represented by the eigenvectors of the averaged flux Jacobian, are allowed to propagate with speeds equal to the corresponding eigenvalues.

The "upwind" direction for each wave is clear in one-dimensional flow: it is either forward or backward, according to the sign of each eigenvalue. In two or three dimensions the direction of wave propagation is not so straightforward since the waves can travel in infinitely many directions. In most current upwind flow-solvers, however, the upwinding direction is taken normal to the cell faces. Thus the schemes are strongly coupled to the grid on which they are implemented, and high resolution of flowfield discontinuities such as shock or shear waves can be achieved only when the discontinuities are aligned with grid lines. The Riemann solver interprets waves incorrectly when they lie oblique to the grid; this improper interpretation can lead to smearing in the numerical solution.

In recent years, in an attempt to improve the accuracy of flow solutions, a number of multidimensional upwind methods have been developed [1, 2, 4–6, 8, 10, 12, 16]. One of the common features of many of these methods is that information needed at special points because of physical considerations must be interpolated from surrounding data points. Since this adds an extra level of complexity to any method, particularly for non-Cartesian meshes, it was decided early in the development of the present scheme to only use information obtained by interpolation along grid lines as the input to the multidimensional approximate Riemann solver. It is then the job of the solver to make "intelligent" use of information gleaned from these left and right states. The solver is handicapped in this task by the limited information to which it has access, but the resulting simplicity and low expense of the method may outweigh its drawbacks.

The current method uses five waves to describe the difference in states at a grid face. Four of these are acoustic, shear, and entropy waves that act in the velocity-difference

0021-9991/93 $5.00

direction (the same dominant direction chosen by Davis [2]), while the fifth is a shear wave that propagates at a right angle to the other four (also used by Parpia and Michalek [8]). This fifth wave allows the method to capture oblique steady shear waves sharply. The method also makes use of the linearizations of the Euler equations due to Roe [11] in order to maintain as simple a scheme as possible. The nature of the wave model makes the method particularly suited for computing steady solutions; there is no experience with the use of the method for simulating transient flows.

1. GOVERNING EQUATIONS

The two-dimensional Navier–Stokes equations can be written in nondimensional form as

$$\frac{\partial \mathbf{U}}{\partial t}+\frac{\partial \mathbf{F}}{\partial x}+\frac{\partial \mathbf{G}}{\partial y}=\frac{\partial \mathbf{F}_v}{\partial x}+\frac{\partial \mathbf{G}_v}{\partial y}, \tag{1.1}$$

where the conserved variables are $\mathbf{U}=[\rho, \rho u, \rho v, \rho E]^T$ and the inviscid flux vectors are

$$\mathbf{F}=\begin{bmatrix} \rho u \\ \rho u^2+p \\ \rho uv \\ \rho uH \end{bmatrix}, \qquad \mathbf{G}=\begin{bmatrix} \rho v \\ \rho uv \\ \rho v^2+p \\ \rho vH \end{bmatrix}. \tag{1.2}$$

The viscous fluxes are

$$\mathbf{F}_v=\begin{bmatrix} 0 \\ \tau_{11} \\ \tau_{21} \\ u_j\tau_{1j}+k\dfrac{\partial T}{\partial x} \end{bmatrix}, \quad \mathbf{G}_v=\begin{bmatrix} 0 \\ \tau_{12} \\ \tau_{22} \\ u_j\tau_{2j}+k\dfrac{\partial T}{\partial y} \end{bmatrix}, \tag{1.3}$$

where

$$\tau_{ij}=\mu\left(\frac{\partial u_i}{\partial x_j}+\frac{\partial u_j}{\partial x_i}\right)+\lambda\frac{\partial u_k}{\partial x_k}\delta_{ij}, \tag{1.4}$$

and λ is taken as $-(\frac{2}{3})\mu$ (Stokes' hypothesis). The ideal gas equation-of-state closes the set of equations:

$$p=(\gamma-1)\rho\left[E-\frac{u^2+v^2}{2}\right]. \tag{1.5}$$

The equations can be discretized in finite-volume form as

$$\frac{\partial \mathbf{U}_{i,j}}{\partial t}=-\frac{1}{A_{i,j}}\left\{\sum_{l=1}^{4}\mathbf{\Phi}_l\,\Delta s_l-\sum_{l=1}^{4}(\mathbf{\Phi}_v)_l\,\Delta s_l\right\}_{i,j} \tag{1.6}$$

$$\mathbf{\Phi}=\begin{bmatrix} \rho q_g \\ \rho q_g u+p\cos\theta_g \\ \rho q_g v+p\sin\theta_g \\ \rho q_g H \end{bmatrix} \tag{1.7}$$

$$\mathbf{\Phi}_v=\begin{bmatrix} 0 \\ \tau_{11}\cos\theta_g+\tau_{12}\sin\theta_g \\ \tau_{21}\cos\theta_g+\tau_{22}\sin\theta_g \\ \left(u_j\tau_{1j}+k\dfrac{\partial T}{\partial x}\right)\cos\theta_g+\left(u_j\tau_{2j}+k\dfrac{\partial T}{\partial y}\right)\sin\theta_g \end{bmatrix}, \tag{1.8}$$

where θ_g is the angle that the outward-pointing cell face normal makes with the x-axis, and q_g is the outward velocity normal to the cell face, given by

$$q_g \equiv u\cos\theta_g+v\sin\theta_g. \tag{1.9}$$

Also, $A_{i,j}$ is the area of the cell (i,j), Δs_l is the length of the lth cell face, and $(\mathbf{\Phi}_v)_l$ is the viscous normal flux per unit face-length, evaluated using central differencing. $\mathbf{\Phi}_l$ is the inviscid normal flux per unit face-length at cell face l, evaluated using a flux function,

$$\mathbf{\Phi}_{m+1/2}=\mathbf{\Phi}[(\mathbf{W}_L)_{m+1/2},(\mathbf{W}_R)_{m+1/2}]. \tag{1.10}$$

Here $\mathbf{W}$ is the vector of primitive variables $\mathbf{W}=[\rho, u, v, p]^T$, m represents the grid index i or j, and $m+\frac{1}{2}$ represents the cell face located between the cell centers m and $m+1$. $\mathbf{W_L}$ and $\mathbf{W_R}$ are obtained at the cell faces via one-point extrapolation for first-order spatial differencing and via a two-point one-sided extrapolation for second-order. The subscripts **L** and **R** denote the directional bias of the extrapolation. The forms of the numerical flux function (1.10) for both the common grid-aligned model and the current grid-independent model are discussed in the next section.

2. THE FLUX FUNCTION

Traveling-Wave Form of the Euler Equations

It is widely supposed that differencing of the inviscid terms is crucial to the treatment of viscous problems; accordingly, the viscous terms are ignored in this section of the paper. The resultant Euler equations can be written in quasilinear form,

$$\frac{\partial \mathbf{W}}{\partial t}+\mathbf{A}\frac{\partial \mathbf{W}}{\partial x}+\mathbf{B}\frac{\partial \mathbf{W}}{\partial y}=0, \tag{2.1}$$

where $\mathbf{W}$ is the vector of primitive variables, and $\mathbf{A}$ and $\mathbf{B}$ are the matrices

$$\mathbf{A}=\begin{bmatrix} u & \rho & 0 & 0 \\ 0 & u & 0 & 1/\rho \\ 0 & 0 & u & 0 \\ 0 & \rho a^2 & 0 & u \end{bmatrix} \tag{2.2}$$

$$\mathbf{B}=\begin{bmatrix} v & 0 & \rho & 0 \\ 0 & v & 0 & 0 \\ 0 & 0 & v & 1/\rho \\ 0 & 0 & \rho a^2 & v \end{bmatrix}. \tag{2.3}$$

Traveling wave solutions to (2.1) are of the form

$$\mathbf{W}(x, y, t)=\mathbf{W}(x\cos\theta + y\sin\theta - \lambda t), \tag{2.4}$$

where θ is the angle that defines the direction of wave propagation. Substitution of (2.4) into (2.1) results in the eigenvalue problem

$$(\mathbf{A}\cos\theta + \mathbf{B}\sin\theta)\,\delta\mathbf{W} = \lambda\delta\mathbf{W}, \tag{2.5}$$

where $\delta\mathbf{W}$ is the amplitude of the traveling wave. The four eigenvalues of (2.5) are

$$\begin{aligned} \lambda_1 &= q + a \\ \lambda_2 &= q - a \\ \lambda_3 &= q \\ \lambda_4 &= q, \end{aligned} \tag{2.6}$$

where q is the component of the velocity in the direction of wave propagation:

$$q \equiv u\cos\theta + v\sin\theta. \tag{2.7}$$

The corresponding right eigenvectors are

$$\begin{aligned} \mathbf{P}_1 &= \left[1, \frac{a}{\rho}\cos\theta, \frac{a}{\rho}\sin\theta, a^2\right]^{\mathrm{T}} \\ \mathbf{P}_2 &= \left[1, -\frac{a}{\rho}\cos\theta, -\frac{a}{\rho}\sin\theta, a^2\right]^{\mathrm{T}} \\ \mathbf{P}_3 &= \left[0, -\frac{a}{\rho}\sin\theta, \frac{a}{\rho}\cos\theta, 0\right]^{\mathrm{T}} \\ \mathbf{P}_4 &= [1, 0, 0, 0]^{\mathrm{T}}. \end{aligned} \tag{2.8}$$

These eigenvectors represent: (1) an acoustic disturbance that propagates with speed λ_1; (2) an acoustic disturbance that propagates with speed λ_2; (3) a shear wave; and (4) an entropy wave. The latter two waves travel with speed $\lambda_3 = \lambda_4$. Together the four eigenvectors form the matrix $\mathbf{P}$.

The characteristic variables for the quasilinear form of the Euler equations can be computed from

$$\delta\mathbf{W}^* = \mathbf{P}^{-1}\,\delta\mathbf{W}, \tag{2.9}$$

yielding

$$\delta\mathbf{W}^* = \begin{bmatrix} \frac{1}{2}\left\{\frac{\delta p}{a^2} + \left(\cos\theta\frac{\rho}{a}\delta u + \sin\theta\frac{\rho}{a}\delta v\right)\right\} \\ \frac{1}{2}\left\{\frac{\delta p}{a^2} - \left(\cos\theta\frac{\rho}{a}\delta u + \sin\theta\frac{\rho}{a}\delta v\right)\right\} \\ -\frac{\rho}{a}\sin\theta\delta u + \frac{\rho}{a}\cos\theta\delta v \\ \delta\rho - \frac{\delta p}{a^2} \end{bmatrix}. \tag{2.10}$$

Rewriting the Euler equations in terms of the characteristic variables gives

$$\frac{\partial\mathbf{W}^*}{\partial t} + \mathbf{P}^{-1}\mathbf{A}\mathbf{P}\frac{\partial\mathbf{W}^*}{\partial x} + \mathbf{P}^{-1}\mathbf{B}\mathbf{P}\frac{\partial\mathbf{W}^*}{\partial y} = 0. \tag{2.11}$$

In general, $\mathbf{A}$ and $\mathbf{B}$ do not commute, so there is no angle θ for which (2.11) is in diagonal form. This is indicative of the fact that in multidimensional flow the waves propagate in infinitely many directions and that for each direction the eigenvectors are distinct. As numerical schemes are limited to modeling the flow with a finite number of waves, the choice of wave type and direction of propagation must be made carefully. The more "physically relevant" the wave types and directions of propagation are, the more likely the model will be able to resolve a wide variety of flow features accurately.

Grid aligned wave models use the grid-normal direction as the direction of wave propagation. By constraining the waves in this way, grid-aligned models misinterpret flowfield structures such as shock or shear waves that lie oblique to meshlines, as described in detail below. We instead seek to improve the flux function by choosing waves that travel in directions dictated by the physics of the local flowfield.

The Grid-Aligned Wave Model

As a motivation for the development of the grid-independent model, the grid-aligned model [11] is reviewed here, including a detailed look at some of the reasons why it misinterprets shock and shear waves that lie oblique to the mesh. This model employs approximate Riemann solutions, in which the flux Jacobian matrix $\mathbf{C} \equiv \partial\mathbf{\Phi}/\partial\mathbf{U}$ is linearized about an averaged state, then the equations are solved exactly in each coordinate direction separately.

Roe-averaged values, derived in [11], are denoted by hats in this paper. The four eigenvectors of the matrix $\hat{\mathbf{C}}$ are

$$\begin{aligned}
\hat{\mathbf{R}}_1 &= [1,\ \hat{u}+\hat{a}\cos\theta_g,\ \hat{v}+\hat{a}\sin\theta_g,\ \hat{H}+\hat{a}\hat{q}_g]^{\mathrm{T}}\\
\hat{\mathbf{R}}_2 &= [1,\ \hat{u}-\hat{a}\cos\theta_g,\ \hat{v}-\hat{a}\sin\theta_g,\ \hat{H}-\hat{a}\hat{q}_g]^{\mathrm{T}}\\
\hat{\mathbf{R}}_3 &= [0,\ -\hat{a}\sin\theta_g,\ \hat{a}\cos\theta_g,\ \hat{a}\hat{r}_g]^{\mathrm{T}}\\
\hat{\mathbf{R}}_4 &= [1,\ \hat{u},\ \hat{v},\ \tfrac{1}{2}(\hat{u}^2+\hat{v}^2)]^{\mathrm{T}},
\end{aligned} \tag{2.12}$$

and represent, respectively, +acoustic, −acoustic, shear, and entropy waves. In (2.12), q is defined by (2.7), and r is defined by

$$r \equiv -u\sin\theta + v\cos\theta. \tag{2.13}$$

The subscript g on the q and r in (2.12) indicates that θ is taken as θ_g, the angle that the grid-normal direction makes with the x-axis. When the equations are written in primitive-variable form, the waves (2.12) are represented by $\mathbf{P}_1$, $\mathbf{P}_2$, $\mathbf{P}_3$, and $\mathbf{P}_4$ in (2.8), with θ taken as θ_g.

The strength $\hat{\Omega}_k$ of each wave arises from satisfying:

$$\Delta\mathbf{U} = \sum_k \hat{\Omega}_k \hat{\mathbf{R}}_k. \tag{2.14}$$

Since the eigenvectors form a basis for the eigenspace of this system, there is always a unique set of strengths that satisfy (2.14). They are, written as components of the vector $\hat{\mathbf{\Omega}}$,

$$\hat{\mathbf{\Omega}} = \begin{bmatrix} \dfrac{1}{2\hat{a}^2}(\Delta p + \hat{\rho}\hat{a}\,\Delta q) \\ \dfrac{1}{2\hat{a}^2}(\Delta p - \hat{\rho}\hat{a}\,\Delta q) \\ \dfrac{1}{\hat{a}}\hat{\rho}\,\Delta r \\ \dfrac{1}{\hat{a}^2}(\hat{a}^2\,\Delta\rho - \Delta p) \end{bmatrix}, \tag{2.15}$$

where $\Delta(\cdot) = (\cdot)_R - (\cdot)_L$. The wavespeeds, which all point normal to the grid face (in the θ_g-direction), are the eigenvalues of $\hat{\mathbf{C}}$:

$$\begin{aligned}
\hat{\lambda}_1 &= \hat{q} + \hat{a}\\
\hat{\lambda}_2 &= \hat{q} - \hat{a}\\
\hat{\lambda}_3 &= \hat{q}\\
\hat{\lambda}_4 &= \hat{q}.
\end{aligned} \tag{2.16}$$

The flux on each grid face is computed using

$$\mathbf{\Phi} = \tfrac{1}{2}(\mathbf{\Phi}_{\mathbf{L}} + \mathbf{\Phi}_{\mathbf{R}}) - \tfrac{1}{2}\sum_{k=1}^{4} |\hat{\lambda}_k|\,\hat{\Omega}_k \hat{\mathbf{R}}_k. \tag{2.17}$$

We will now give a geometric interpretation of the grid-aligned model. This will be useful later also in describing alternative models. The difference in states at an interface can be represented in $(\Delta u, \Delta v, \Delta p)$-space by placing L, the representation of the state to the left of the interface, at the origin, and the right state R at $(\Delta u, \Delta v, \Delta p)$. The grid-aligned model assumes that this change is due to waves travelling along the grid-normal. Each such wave can be represented by a line parallel to one of the eigenvectors (2.8), with θ chosen as θ_g. For example, if the difference in states really was due to a single acoustic wave of the + family, R would be found somewhere along the heavy line in Fig. 1a. Note that both acoustic waves lie in the plane $(\Delta u/\Delta v) = \cot\theta_g$. (Since this is a linearized model, all wave paths are straight lines.) A difference due solely to a shear wave travelling along the grid-normal would place the point R in the plane $\Delta p = 0$ and, also, in the plane $(\Delta u/\Delta v) = -\tan\theta_g$, which lies at right angles to the plane shown in the figure. The effect of an entropy wave is not representable in $(\Delta u, \Delta v, \Delta p)$-space.

In the grid-aligned model, an arbitrary jump from L to R will be represented uniquely as the sum of three jumps, each parallel to one of three eigenvectors. It will only rarely be

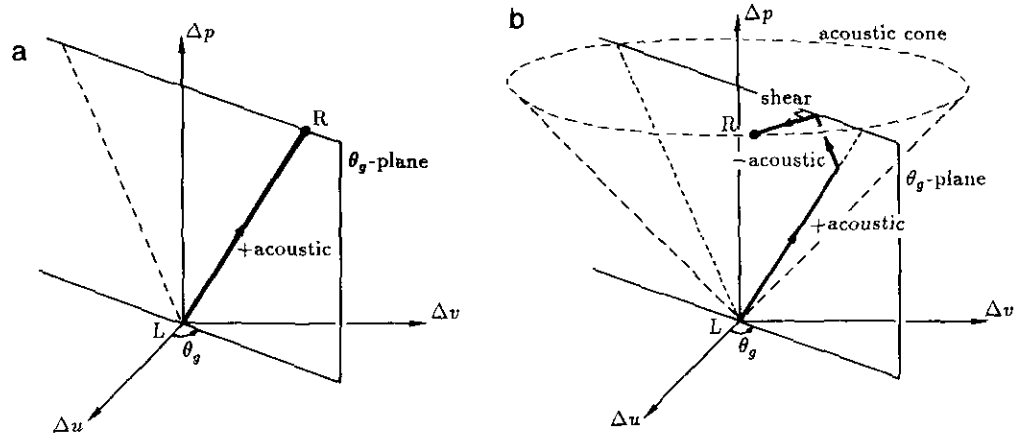

FIG. 1. Grid-aligned wave model interpretations of a single shock wave: (a) aligned with grid; (b) oblique to grid.

the case that such a representation is truly appropriate. For example, in Fig. 1b we show the case where the jump from L to R is caused by a single acoustic wave *not* aligned with the grid. Such a jump (see (2.8)) must lie along a generator of the "acoustic cone"

$$(\Delta p)^2 = \rho^2 a^2((\Delta u)^2 + (\Delta v)^2). \tag{2.18}$$

The grid-aligned model will represent the jump by the path shown, which includes a shear wave as well as an acoustic wave of the opposite family. These extra waves add dissipation which smears the numerical solution.

The grid-aligned flux function can also misinterpret a pure shear wave that lies oblique to a grid face. This situation is illustrated in Fig. 2. In Fig. 2a, left and right states are indicated on a $(\Delta u, \Delta v, \Delta p)$-diagram. There is no pressure difference between L and R, and the velocity-difference vector $\mathbf{V}_R - \mathbf{V}_L$ is at some angle other than 90° to the θ_g-direction. (It would be normal to the θ_g-direction for a shear wave aligned with the grid face, in which case the wave model would interpret the difference correctly with a single shear wave.) The grid-aligned scheme now includes two acoustic waves in its interpretation of the difference in states. These waves add dissipation which smears the numerical solution. Additionally, if the wavespeeds associated with each of these acoustic waves are of opposite sign, then the scheme computes a flux at the interface with a pressure that is different from the correct pressure by an amount Δp, as shown in Fig. 2b. In this figure, a time history of the wave locations is drawn in relation to the grid-normal direction. The flux at the interface is computed as either the left flux plus the change across left-running waves or, equivalently, the right flux minus the change across the right-running waves. In either case it can be seen that the incorrect pressure is given at the interface.

The Grid-Independent Wave Model

The motivation behind the development of the present grid-independent approximate Riemann solver is the desire to be able to recognize and appropriately model both shock and shear waves regardless of their orientation with respect to the grid. The method for accomplishing this goal is the following: (1) choose a direction of wave propagation more physically appropriate than the directions defined by the grid, (2) represent the difference in L and R states with a combination of acoustic, shear, and entropy waves, and (3) form a flux *in the grid direction* from the information propagating in the physically relevant grid-independent direction.

The primary wave propagation direction used at each interface is the velocity-difference direction

$$(\theta_d)_{m+1/2} = \tan^{-1}\left(\frac{v_{m+1} - v_m}{u_{m+1} - u_m}\right), \tag{2.19}$$

defined from $-\pi/2$ to $\pi/2$, where m represents the grid index i or j. This is the angle that the velocity-difference vector, $\mathbf{V}_{m+1} - \mathbf{V}_m$, makes with the x-axis. The θ_d-direction is chosen because in this frame the velocity components $\bar{v}_L$ and $\bar{v}_R$ normal to θ_d are equal, as depicted in Fig. 3. Therefore the differences between the two states can be interpreted either as a compression normal to θ_d or a shear aligned with θ_d. In Fig. 4a, the former interpretation is illustrated. The velocity components tangential to the shock are equal (only the normal component is affected by the shock). The shock wave could be propagating with some velocity $\bar{u}_S$ in the θ_d-direction. The value of $\bar{u}_S$ is zero for a steady shock wave. A shear-wave interpretation of the difference in velocities is illustrated in Fig. 4b. Here, the shear wave propagates with velocity $\bar{v}_L = \bar{v}_R$ in the $(\theta_d + \pi/2)$-direction. This propagation velocity is zero for a steady shear wave.

Since there are two interpretations of a velocity difference in terms of a dominant wave, it is necessary that the method be able to model both types as well as have some way of determining which is a better description of the true situation. The present method models both types by describing the difference in states by a combination of two acoustic waves and an entropy wave propagating in the

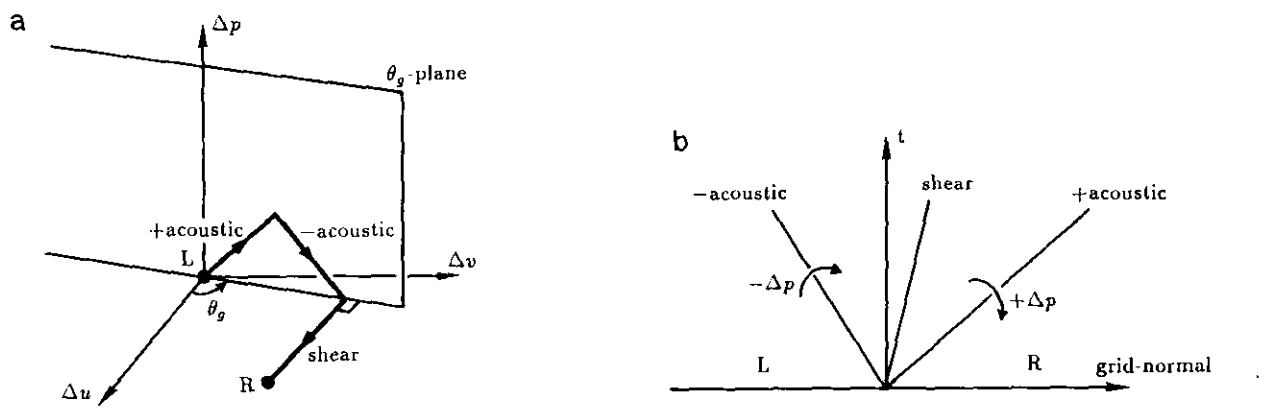

FIG. 2. Grid-aligned wave model interpretation of an oblique shear wave: (a) wave decomposition; (b) wave directions for subsonic flow.

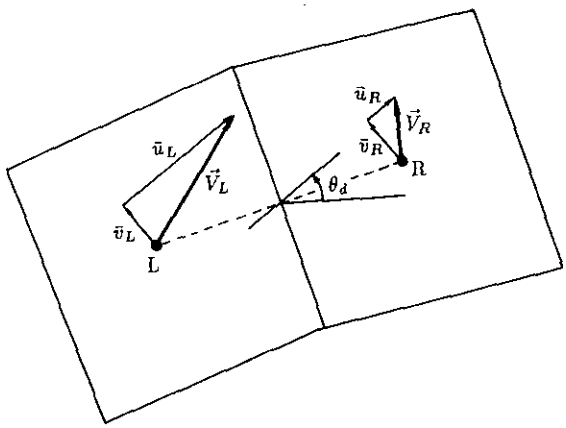

FIG. 3. Components of $\mathbf{V}_L$ and $\mathbf{V}_R$ in the θ_d-frame.

θ_d-direction and an additional shear wave propagating in the $(\theta_d + \pi/2)$-direction. This shear wave causes a change in velocity *parallel* to θ_d with no change in pressure, thus allowing for sharp capturing of oblique shear waves of the type depicted in Fig. 4b.

The representation in primitive-variable form of the θ_d acoustic waves and entropy wave are simply $\mathbf{P}_1$, $\mathbf{P}_2$, and $\mathbf{P}_4$ from (2.8) with θ taken as θ_d. The $(\theta_d + \pi/2)$ shear wave is represented by $\mathbf{P}_3$ with $\theta = \theta_d + \pi/2$:

$$\mathbf{P}_{(\theta_d+\pi/2)\text{shear}} = \begin{bmatrix} 0 \\ -\frac{a}{\rho}\sin\left(\theta_d+\frac{\pi}{2}\right) \\ \frac{a}{\rho}\cos\left(\theta_d+\frac{\pi}{2}\right) \\ 0 \end{bmatrix} = \begin{bmatrix} 0 \\ -\frac{a}{\rho}\cos\theta_d \\ -\frac{a}{\rho}\sin\theta_d \\ 0 \end{bmatrix}. \tag{2.20}$$

The strengths of the four waves must still satisfy (2.14), where the $\hat{\mathbf{R}}_k$ now represent the grid-independent waves for the conserved-variable form of the equations:

$$\begin{aligned} \hat{\mathbf{R}}_1 &= [1,\ \hat{u} + \hat{a}\cos\theta_d,\ \hat{v} + \hat{a}\sin\theta_d,\ \hat{H} + \hat{a}\hat{q}_d]^{\mathrm{T}} \\ \hat{\mathbf{R}}_2 &= [1,\ \hat{u} - \hat{a}\cos\theta_d,\ \hat{v} - \hat{a}\sin\theta_d,\ \hat{H} - \hat{a}\hat{q}_d]^{\mathrm{T}} \\ \hat{\mathbf{R}}_3 &= [0,\ -\hat{a}\cos\theta_d,\ -\hat{a}\sin\theta_d,\ -\hat{a}\hat{q}_d]^{\mathrm{T}} \\ \hat{\mathbf{R}}_4 &= [1,\ \hat{u},\ \hat{v},\ \tfrac{1}{2}(\hat{u}^2 + \hat{v}^2)]^{\mathrm{T}}. \end{aligned} \tag{2.21}$$

These vectors represent, respectively, $+\theta_d$ acoustic, $-\theta_d$ acoustic, $(\theta_d + \pi/2)$ shear, and entropy waves. The hatted variables are still Roe-averaged variables, and the subscript d on the q indicates that θ is taken as θ_d in (2.7). Note that the acoustic and shear waves in (2.21) all cause a change in velocity in the θ_d-direction only; there is no equivalent to the grid-aligned shear wave $\hat{\mathbf{R}}_3$ from (2.12) to account for differences in velocity in any other direction. The reason for this is that, by definition, the states L and R are separated by a velocity difference in the θ_d-direction exactly, so there is no need for any other wave.

Unlike in the grid-aligned method, there is not a unique combination of these four waves that satisfies (2.14) since (2.21) are not all linearly independent. It turns out that the entropy wave always has a strength of $\hat{\Omega}_4 = \Delta\rho - \Delta p/\hat{a}^2$, but there is some freedom in picking the strengths of the other three waves. This reflects, as mentioned earlier, that there are two types of dominant waves, represented by Figs. 4a and b, that could describe the difference in states. The model must choose which type is more likely to be representative of the true situation and allow that type of wave to dominate in the numerical representation.

Two methods that allow the model to choose the "correct" wave type are described here. Both are a function of the pressure difference across the interface: if a large pressure difference exists, it is more likely that an acoustic wave is primarily responsible for the difference in states. Similarly, a small difference in pressure indicates that a shear wave more likely is the primary wave.

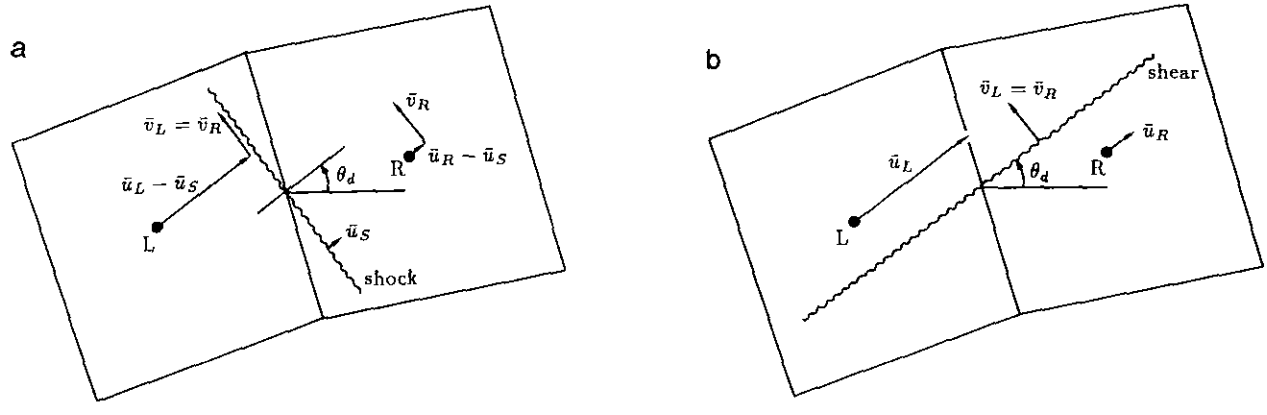

FIG. 4. Interpretations of velocity difference: (a) shock; (b) shear.

The first method is termed the minimum-pathlength model and is implemented by choosing the combination of waves such that the pathlength in $(\Delta u, \Delta v, \Delta p)$-space is minimized. This minimum-pathlength model is accomplished by using either two acoustic waves and an entropy wave or one acoustic, a $(\theta_d + \pi/2)$ shear, and an entropy wave. (Recall that the entropy wave is not representable in $(\Delta u, \Delta v, \Delta p)$-space, but its strength is $\Delta\rho - \Delta p/\hat{a}^2$ independently of the way the remaining waves are allocated.) The choice of path depends on the location in phase space of the right state R relative to the cone defined by all acoustic waves emanating from L. By definition, R lies in the θ_d-plane. If R resides inside the "acoustic cone," as is the case with R_1 in Fig. 5, then two acoustic waves describe the shortest path. If R resides outside the cone, as represented by R_2 in the figure, then one acoustic and a $(\theta_d + \pi/2)$ shear wave describe the shortest path. The mathematical conditions for R inside or outside the acoustic cone are

$$\text{Inside: } (\Delta p)^2 \geqslant [\hat{\rho}\hat{a}(\Delta u \cos\theta_d + \Delta v \sin\theta_d)]^2 \tag{2.22}$$

$$\text{Outside: } (\Delta p)^2 < [\hat{\rho}\hat{a}(\Delta u \cos\theta_d + \Delta v \sin\theta_d)]^2. \tag{2.23}$$

The minimum-pathlength model always uses three waves out of a choice of four possible wave types to describe the difference in states.

A second strategy, due to Parpia and Michalek [9], is to choose the strengths of the acoustic and shear waves such that the path is in some sense *closest* to the straight line connecting L and R in phase space. More specifically, the area between the waves (taken in a certain order) and the direct path $L - R$ is minimized. A geometric representation is given in Fig. 6, where again the entropy wave, although present, is not pictured. If R lies inside the acoustic cone, like R_1 in the figure, then the path that minimizes the area (shaded region) is accomplished by two acoustic waves. If R lies outside the cone, as represented by R_2, then some combination of two acoustic waves and a $(\theta_d + \pi/2)$ shear wave gives the minimum area. The exact expression will be given below. The minimum-area model uses either three or four waves to describe the difference in states at each interface.

The grid-independent model, using either the minimum-pathlength or minimum-area variation, automatically describes a pure shock wave at an interface with essentially a single acoustic wave, regardless of the orientation of the discontinuity with respect to the grid. Similarly, a pure shear wave at an interface is modeled with essentially a single $(\theta_d + \pi/2)$ shear wave. Hence this model avoids the problems depicted in Figs. 1b and 2 that the grid-aligned model encounters when it models shock or shear waves that lie oblique to the grid. Through this more accurate modeling, more accurate computed solutions should arise.

Unfortunately, numerical experiments show that the grid-independent wave model can produce nonlinear feedback that results in oscillatory flowfields. Small changes in the computed values of θ_d can feed back into the solution, producing further changes in θ_d. An easy way to inhibit this feedback, applicable if the flow solver is used to march to a steady solution, is to freeze the θ_d values at each face at some point in the computation, calling these θ'_d. The four wave vectors in (2.21) remain the same, only with θ'_d replacing θ_d. Since the state R does not necessarily lie in the θ'_d-plane, at least one additional wave is now needed to account for a velocity difference *out* of the θ'_d-plane. A shear wave

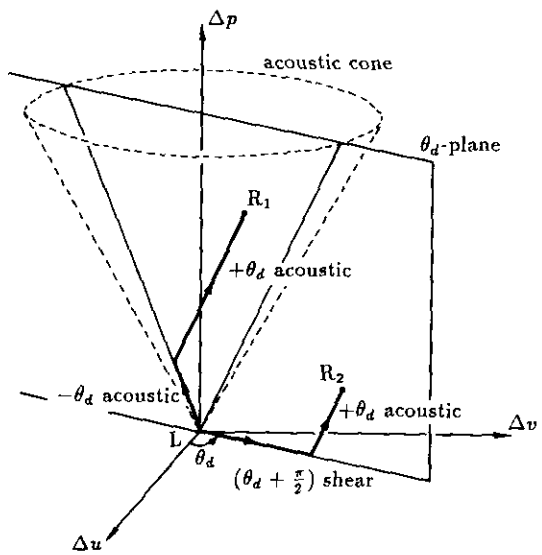

FIG. 5. Minimum-pathlength model wave decomposition (entropy wave not pictured).

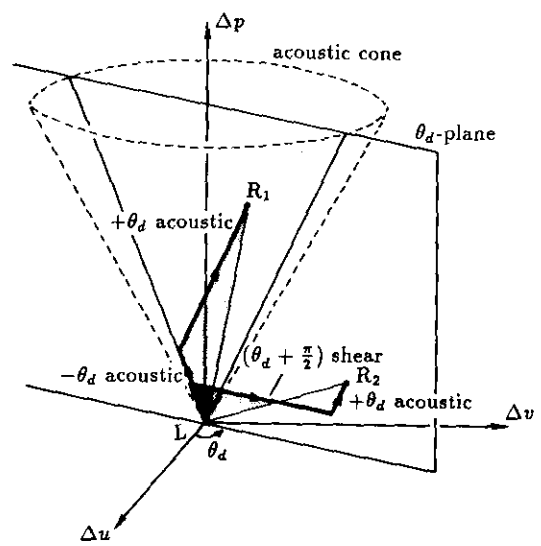

FIG. 6. Minimum-area model wave decomposition (entropy wave not pictured).

propagating in the θ'_d-direction produces a change in velocity *normal* to θ'_d and can therefore be used as the additional wave. It is represented by

$$\hat{\mathbf{R}}_5 = [0,\ -\hat{a}\sin\theta'_d,\ \hat{a}\cos\theta'_d,\ \hat{a}(-\hat{u}\sin\theta'_d + \hat{v}\cos\theta'_d)]^{\mathrm{T}}. \tag{2.24}$$

Some loss of resolution may be expected to go hand in hand with the freezing of the wave-propagation directions. However, through the careful choice of a freezing procedure, it turns out that this loss is very small. One procedure that works well is to recompute θ'_d at each grid interface once every fixed number of iterations until a certain level of convergence is reached. After this, θ'_d remains frozen. A second procedure is to simply initiate the grid-independent computation from a converged grid-aligned solution, with θ'_d frozen thereafter.

The combination of the four waves from (2.21) (with θ_d taken as θ'_d) plus the θ'_d shear wave (2.24) results in a model that employs five waves, which can be used to generate a family of flux formulas with a free parameter β. This family includes both the minimum-pathlength and minimum-area models discussed above. The wavestrengths that satisfy (2.14) are taken as

$$\hat{\boldsymbol{\Omega}} = \begin{bmatrix} \dfrac{\Delta p}{2\hat{a}^2} + \beta\dfrac{\hat{\rho}}{2\hat{a}}(\Delta u\cos\theta'_d + \Delta v\sin\theta'_d) \\ \dfrac{\Delta p}{2\hat{a}^2} - \beta\dfrac{\hat{\rho}}{2\hat{a}}(\Delta u\cos\theta'_d + \Delta v\sin\theta'_d) \\ (\beta-1)\dfrac{\hat{\rho}}{\hat{a}}(\Delta u\cos\theta'_d + \Delta v\sin\theta'_d) \\ \dfrac{1}{\hat{a}^2}(\hat{a}^2\,\Delta\rho - \Delta p) \\ \dfrac{\hat{\rho}}{\hat{a}}(-\Delta u\sin\theta'_d + \Delta v\cos\theta'_d) \end{bmatrix}. \tag{2.25}$$

The minimum-pathlength model is obtained when

$$\beta = \min\left[\left|\frac{\Delta p/(\hat{\rho}\hat{a})}{\Delta u\cos\theta'_d + \Delta v\sin\theta'_d}\right|, 1\right]. \tag{2.26}$$

In this case, the grid-independent model uses only four waves at a time since either the $(\theta'_d + \pi/2)$ shear wave-strength or one of the acoustic wavestrengths is identically zero. The minimum-area model results when

$$\beta = \min\left[\left\{\frac{\Delta p/(\hat{\rho}\hat{a})}{\Delta u\cos\theta'_d + \Delta v\sin\theta'_d}\right\}^2, 1\right], \tag{2.27}$$

and the model uses all five waves when R lies outside the acoustic cone, and four waves when R lies inside the acoustic cone (the $(\theta'_d + \pi/2)$ shear strength is zero). Derivations of these two expressions (2.26) and (2.27) can be found in Rumsey [15]. In practice, a small number ε is added to the denominators to avoid division by zero in regions of null gradient. Also, β is generally limited to be no less than 0.05, and is frozen along with θ'_d as an aid to convergence.

Numerical experiments indicate that both the minimum-pathlength and the minimum-area models give very similar results, although the minimum-area model tends to be slightly more dissipative for a wider range of test cases. Hence, it exhibits less oscillatory behavior and usually converges slightly faster. The minimum-area model is used for all the computations in this paper.

In spite of the fact that there is no rigorous justification for its use in the grid-independent model, the "standard" flux formula

$$\boldsymbol{\Phi} = \tfrac{1}{2}(\boldsymbol{\Phi}_{\mathbf{L}} + \boldsymbol{\Phi}_{\mathbf{R}}) - \tfrac{1}{2}\sum_{k=1}^{5} |\hat{\lambda}_k|\,\hat{\Omega}_k\hat{\mathbf{R}}_k \tag{2.28}$$

is used to obtain the flux per unit face-length normal to each grid face. This formula is the average of the two expressions:

$$\begin{aligned} \boldsymbol{\Phi} &= \boldsymbol{\Phi}_{\mathbf{L}} + \sum_{\hat{\lambda}<0} \hat{\lambda}_k\hat{\Omega}_k\hat{\mathbf{R}}_k \\ \boldsymbol{\Phi} &= \boldsymbol{\Phi}_{\mathbf{R}} - \sum_{\hat{\lambda}>0} \hat{\lambda}_k\hat{\Omega}_k\hat{\mathbf{R}}_k. \end{aligned} \tag{2.29}$$

Hence it may be argued that it is correct because of its symmetry—it favors neither input state—but this reasoning is merely heuristic. An attempt was made in [15] to justify the use of (2.28) based on comparisons with a different formulation of the model, but, from a theoretical standpoint, the issue still remains unresolved.

The wavespeeds $\hat{\lambda}_k$ are taken as the components of the individual wavespeeds in the θ_g-direction:

$$\begin{aligned} \hat{\lambda}_1 &= (\hat{q}'_d + \hat{a})\cos(\theta'_d - \theta_g) \\ \hat{\lambda}_2 &= (\hat{q}'_d - \hat{a})\cos(\theta'_d - \theta_g) \\ \hat{\lambda}_3 &= \hat{r}'_d\{-\sin(\theta'_d - \theta_g)\} \\ \hat{\lambda}_4 &= \hat{q}'_d\cos(\theta'_d - \theta_g) \\ \hat{\lambda}_5 &= \hat{q}'_d\cos(\theta'_d - \theta_g). \end{aligned} \tag{2.30}$$

Note that the grid-independent model reduces to the grid-aligned approximate Riemann solver when $\theta'_d = \theta_g$ and $\beta = 1$ (i.e., the $(\theta'_d + \pi/2)$ shear-strength vanishes).

It is worth noting at this point that, although it is reasonable to search for single waves that are not necessarily aligned with the grid face to "explain" a transition between two states, the finite-volume scheme itself is unable in general to preserve an oblique discontinuity

exactly once it is found. Conservative difference schemes are based on cell averages of the solution, rather than point samples, and their nature is to spread the discontinuity over a strip of cells. It is hoped though, through the application of the relatively simple grid-independent model, that oblique discontinuities (while not preserved exactly) will be resolved more accurately than those obtained using the grid-aligned model.

Stability and Monotonicity

A linearized stability analysis [13, 15] of the grid-independent model in conjunction with the two-dimensional Euler equations, advanced in time using explicit time-marching, shows that some modes of the Fourier footprint contain eigenvalues that lie on the imaginary axis. Hence the stability boundary of the time-marching scheme must include a finite portion of the imaginary axis as well. Explicit forward-Euler time-stepping does not satisfy this requirement, but multistage schemes can. The four-stage scheme,

$$\begin{aligned}
\mathbf{U}^{(1)} &= \mathbf{U}^{(n)} + \frac{\eta\,\Delta t}{A}\left(\sum_l \mathbf{\Phi}_l\,\Delta s_l\right)^{(n)} \\
\mathbf{U}^{(2)} &= \mathbf{U}^{(n)} + \frac{\Delta t}{3A}\left(\sum_l \mathbf{\Phi}_l\,\Delta s_l\right)^{(1)} \\
\mathbf{U}^{(3)} &= \mathbf{U}^{(n)} + \frac{\Delta t}{2A}\left(\sum_l \mathbf{\Phi}_l\,\Delta s_l\right)^{(2)} \\
\mathbf{U}^{(n+1)} &= \mathbf{U}^{(n)} + \frac{\Delta t}{A}\left(\sum_l \mathbf{\Phi}_l\,\Delta s_l\right)^{(3)},
\end{aligned} \tag{2.31}$$

with $\eta = 0.15$, is stable up to CFL numbers of about 1.75 for first-order spatial accuracy and 0.87 for second order. These results are dependent on the Mach number; the maximum allowable CFL numbers are generally higher than this when M is of order 1. For example, at $M = 3$ the maximum CFL numbers are about 2.2 for first order and 1.3 for second order.

The grid-independent model in an implicit approximate-factorization algorithm is stable only up to a CFL number of about 2.5 for first-order and 0.3 for second order when first-order-accurate grid-aligned approximate Jacobians are employed on the left-hand side. Again these CFL numbers are dependent on Mach number. Typical limits for Mach numbers of order 1 are about 4 for first-order spatial accuracy and 2 for second-order. When appropriate grid-independent left-hand side approximate Jacobians are employed, first-order computations are unconditionally stable. Similarly, second-order computations are unconditionally stable according to the linearized analysis if block-pentadiagonal systems (as opposed to tridiagonal systems) are solved with appropriately chosen grid-independent approximate Jacobians. Maximum CFL numbers of about 100 can be attained in practice with this strategy, although the optimum CFL number for convergence generally lies between about 2 and 6.

A linearized monotonicity analysis is used to investigate the monotonicity properties of the grid-independent model. The analysis is derived from considerations of the one-dimensional Euler equations:

$$\frac{\partial \mathbf{U}}{\partial t} + \mathbf{A}\frac{\partial \mathbf{U}}{\partial x} = 0. \tag{2.32}$$

These equations can be diagonalized into three nonlinearly coupled equations, each which describes the convection of a characteristic variable W_k:

$$\frac{\partial \mathbf{W}}{\partial t} + \mathbf{P}^{-1}\mathbf{A}\mathbf{P}\frac{\partial \mathbf{W}}{\partial x} = 0. \tag{2.33}$$

The numerical scheme to advance each W_k can be written

$$(W_k)_i^{(n+1)} = \sum_{m=-l}^{l} (c_k)_m\,(W_k)_{i+m}^{(n)}, \tag{2.34}$$

where $l = 1$ for a scheme with a three-point stencil. From Godunov [3], we know the scheme (2.34) is monotone if all of the coefficients $(c_k)_m$ are greater than or equal to zero. Or, stated differently, the scheme for this diagonalized system of equations is monotone if

$$\text{e.v.}\left(\frac{\partial \mathbf{W}_i^{(n+1)}}{\partial \mathbf{W}_{i+m}^{(n)}}\right) = \text{e.v.}\begin{bmatrix} (c_1)_m & 0 & 0 \\ 0 & (c_2)_m & 0 \\ 0 & 0 & (c_3)_m \end{bmatrix} \geqslant 0, \tag{2.35}$$

for $m = -l, \ldots, 0, \ldots, l$, and e.v.$(\cdot)$ represents the eigenvalues of $(\cdot)$. But the matrix $\partial \mathbf{U}_i^{(n+1)}/\partial \mathbf{U}_{i+m}^{(n)}$, termed the "influence matrix," is similar to the matrix in (2.35) and hence has the same eigenvalues. So

$$\text{e.v.}\left(\frac{\partial \mathbf{U}_i^{(n+1)}}{\partial \mathbf{U}_{i+m}^{(n)}}\right) \geqslant 0, \qquad m = -l, \ldots, 0, \ldots, l, \tag{2.36}$$

represents an equivalent monotonicity condition for the one-dimensional Euler equations. It turns out that the condition when $m = 0$ can be eliminated from (2.36) since $\partial \mathbf{U}_i^{(n+1)}/\partial \mathbf{U}_i^{(n)} \geqslant 0$ acts merely to limit the time step.

The monotonicity analysis of the two-dimensional Euler equations is not as straightforward, since the equations are not simultaneously diagonalizable in both coordinate directions. However, we proceed by diagonalizing *one* of the

coordinate directions, and we ignore the influence matrix from the other direction. This translates into the condition

$$\text{e.v.}\left(\frac{\partial \mathbf{U}_{i,j}^{(n+1)}}{\partial \mathbf{U}_{k}^{(n)}}\right) \geqslant 0, \qquad k=(i+1,j),(i-1,j), \tag{2.37}$$

for a scheme in which the update at each cell is governed by the computational stencil made up of the points (i,j), $(i+1,j)$, $(i-1,j)$, $(i,j+1)$, and $(i,j-1)$. In practice the eigenvalues may be complex, in which case we apply (2.37) to the real part only. This is only a localized analysis in the particular coordinate direction considered. It is not clear what the combined effects of the monotonicity property (2.37) and the property in the other coordinate direction are. Nonetheless, this approach is utilized to help define a limiting procedure for reducing oscillations in two-dimensional solutions. Details can be found in [14, 15].

The grid-independent model is shown in [14, 15] to be non-monotone in general for even first-order spatial accuracy. However, the oscillations that occur near discontinuities can be reduced in magnitude to "acceptable" levels for a wide variety of problems by limiting the wave-propagation (θ'_d) directions according to a strategy suggested by the linearized analysis. This gain in reduced oscillatory behavior does result in the loss of some of the high resolution of oblique shock and shear waves, although the resolution is still generally greater than results using the grid-aligned scheme. Limiting of the θ'_d-direction is also necessary to avoid odd–even point decoupling in boundary layers for viscous flows. This condition occurs on grid-interfaces that are aligned with the flow-direction and is due to the fact that the θ'_d-direction lies approximately along the grid-face so that all grid-normal components of the θ'_d-wavespeeds are nearly zero. Furthermore, the $(\theta'_d+\pi/2)$ shear wave has a very small wavespeed, so the dissipation is also very small and the result is essentially central-differencing across the boundary layer.

Extension to Three Dimensions

The extension of this model to three dimensions is straightforward. The velocity-difference direction is again used as the primary wave-propagation direction. It is denoted by the direction vector $\mathbf{n}_d$, defined by the polar-coordinate angles,

$$(\theta_d)_{m+1/2} = \tan^{-1}\left(\frac{v_{m+1}-v_m}{u_{m+1}-u_m}\right)$$

$$(\psi_d)_{m+1/2} = \tan^{-1}\left(\frac{(w_{m+1}-w_m) * \operatorname{sign}(u_{m+1}-u_m)}{\sqrt{(u_{m+1}-u_m)^2+(v_{m+1}-v_m)^2}}\right), \tag{2.38}$$

at cell face $m+\frac{1}{2}$, where m represents the grid index i, j, or k. These angles are each defined from $-\pi/2$ to $\pi/2$. As in two dimensions, the direction of wave propagation is frozen as $\mathbf{n}'_d$ in order to eliminate nonlinear feedback in the solution, and the end result is again a five-wave model.

All of the waves except for the $(\mathbf{n}'_d+\pi/2)$ shear wave (the three-dimensional equivalent to the $(\theta'_d+\pi/2)$ shear wave) have wavespeeds in the $\mathbf{n}'_d$-direction. The direction in which the $(\mathbf{n}'_d+\pi/2)$ shear wave itself should be allowed to propagate is somewhat unclear since, in three dimensions, there are an infinite number of directions normal to the $\mathbf{n}'_d$-direction. However, in order for the model to be able to sharply capture oblique shear waves through which the velocity undergoes rotation, the propagation direction is taken as the direction normal to the plane spanned by $\mathbf{V}_L$ and $\mathbf{V}_R$. The velocity of this particular shear wave is then identically zero when the direction of wave-propagation is not frozen. When the direction *is* frozen, then the velocity may have some (usually small) finite value.

An empirical angle-limiting method for reducing oscillations near computed shock and shear waves has not been devised for three-dimensional flow due to its inherent complexity. However, it has been found in general that the extra degree of freedom in three dimensions seems to relieve some of the oscillation problems present in two dimensions when the grid-independent model is used.

3. NUMERICAL RESULTS

All computations are performed on the Cray 2 computer at NASA Langley Research Center. Except for the oblique shock reflection case, all computations are performed using the implicit approximate-factorization time-stepping procedure, and convergence is assumed to be reached when the L_2-norm of the residual of the equations drops by at least four orders of magnitude and/or the lift and drag values settle down and do not vary significantly with further iterations. Per iteration, the Euler/Navier–Stokes solver with the grid-independent flux function employed is about 1.5 times more costly than when the grid-aligned flux function is employed. A significant percentage of this cost is associated with the limiting of the θ'_d-directions. Without θ'_d-limiting, the grid-independent model is about 1.2 times more costly than the grid-aligned model per iteration.

In addition to the increased cost per iteration, the grid-independent model also generally requires more iterations than the grid-aligned model to reach the same level of convergence. Based on the convergence criteria given above, it is difficult to give precise comparisons between the methods. However, for shock-reflection calculations, given below, the grid-independent model requires roughly 1.2 times as many iterations as the grid-aligned model for first-order-accurate solutions and roughly 1.6 times as many for second order to drive the L_2-norm of the residual to 1×10^{-12}.

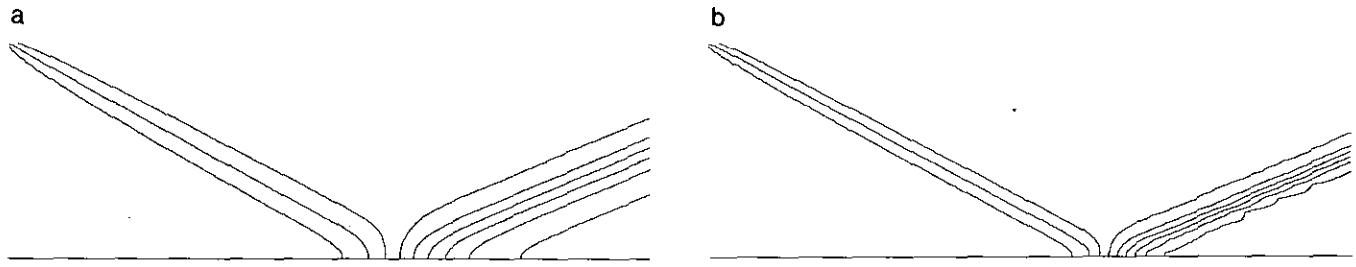

FIG. 7. Pressure contours for oblique shock reflection, first-order, 97×33 grid: (a) grid-aligned; (b) grid-independent.

Oblique Shock Reflection

The Euler equations are used to compute the supersonic flow ($M = 2.9$) over a flat plate with an oblique shock wave reflecting off its surface (the flow is turned through an angle of 10° by the incident shock). Computations are performed on a 97×33 Cartesian mesh. First-order results using both the grid-aligned and grid-independent models are shown in Fig. 7 in plots of nondimensional pressure contours, plotted from 1.2 to 3.6 in increments of 0.3. The grid-independent model resolves the shocks significantly better than the grid-aligned model, and results appear to be monotone as well for this problem.

In Fig. 8, second-order computations (with no limiting of higher-order terms) show the grid-independent results to be only marginally sharper than the grid-aligned results. Also, there are small oscillations present in the grid-independent solution downstream of the reflected shock which show up in the pressure contours as "bubbles" and "kinks." The convergence histories of the first- and second-order grid-aligned and grid-independent schemes using explicit four-stage time-marching (2.31) are shown in Fig. 9.

Supersonic Flow over an Airflow

Several Euler computations are shown for the NACA 0012 airfoil at $M = 1.2$, $\alpha = 0°$ on a 257×73 O-mesh with an outer boundary extent of 20 chords and an average minimum spacing at the body of 0.0031 chords. At these conditions, the NACA 0012 airfoil has a flowfield with a curved bow shock located in front of the airfoil and oblique shocks emanating from the trailing edge. Figure 10 shows nondimensional pressure contours, plotted in increments of 0.05 (the freestream value of 1.0 is not plotted), for the grid-aligned and grid-independent models using first-order spatial accuracy. The shock waves are captured much more sharply by the grid-independent method. However, in spite of the fact that the θ'_d wave-propagation directions are limited in an effort to reduce oscillations, there are still some small oscillations present behind the bow shock.

Second-order computations using the grid-aligned and grid-independent models (with no limiting of higher-order terms) are given in Fig. 11. The grid-independent results are still somewhat sharper than the grid-aligned results, but the difference is not so marked as for first-order. Again there are noticeable oscillations near the bow shock in the grid-independent computation.

Subsonic Flow over an Airfoil

A grid-convergence study is performed using the Euler equations for subsonic flow over an airfoil in order to investigate the effect of the grid-independent model on an airfoil flowfield where no shock waves are present. The conditions are $M = 0.3$ and $\alpha = 1°$, and results are computed on three grids. The finest of these is the same 257×73 O-mesh used in the supersonic flow calculations, and the two coarser meshes are achieved by removing every other point from the next finest mesh.

Figure 12 is a plot of computed drag coefficient versus the inverse of the square root of the grid density for the grid-

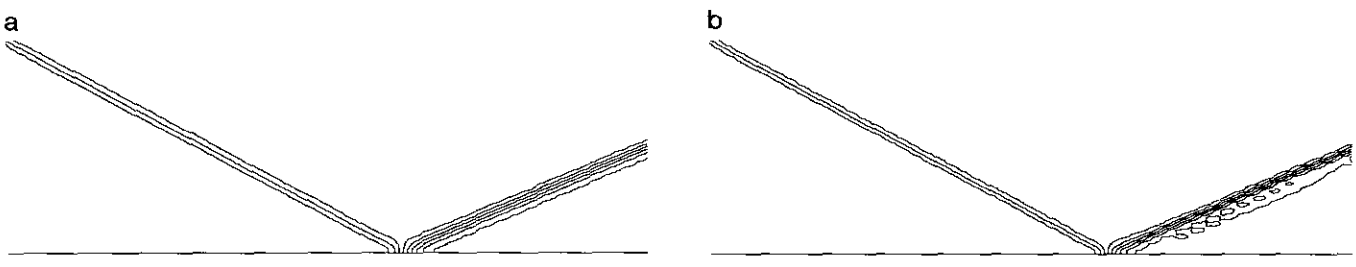

FIG. 8. Pressure contours for oblique shock reflection, second-order, 97×33 grid: (a) grid-aligned; (b) grid-independent.

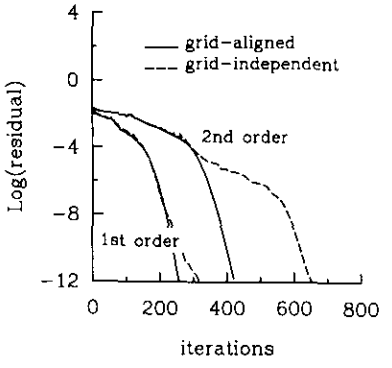

FIG. 9. Convergence histories for oblique shock reflection, 97×33 grid.

aligned model and the grid-independent model on the three grids using first-order spatial discretization. The "exact" Euler solution should give zero drag. The grid-independent model gives a far better prediction of the drag than the grid-aligned scheme for all three grids. Entropy contours (where entropy is defined as $p/(\rho^\gamma) - 1$) for both methods are given in Figs. 13 and 14 on the coarsest and finest meshes. Contour values plotted are in increments of 0.001 for all figures. These figures indicate significantly lower entropy production over the airfoil surface using the grid-independent model. The maximum entropy values for the grid-aligned model are 0.0303, 0.0251, and 0.0183 for the coarsest through finest meshes, respectively. For the grid-independent model the maximum values are only 0.0052, 0.0028, and 0.0018.

It is believed that the difference in entropy levels is due to the different ways that the two models interpret the flow near the stagnation point of the airfoil. Near the stagnation point, the flow undergoes very rapid turning with relatively small changes in pressure. The grid-aligned model interprets this turning to be in part due to the action of acoustic waves, as discussed earlier (Fig. 2). Because the local flow is subsonic, these acoustic waves cause the pressure at interfaces near the leading edge to be computed incorrectly, resulting in increased entropy generation there. In contrast, the grid-independent model interprets the rapid turning near the stagnation point to be due primarily to the action of $(\theta'_d + \pi/2)$ shear waves, which have no associated pressure jump across them. Numerical entropy generation is lower as a consequence.

Although not shown, the grid-aligned and grid-independent models produce results that are very similar to each other in a second-order spatially accurate computation for this configuration. Hence there does not appear to be a significant advantage to using the grid-independent model over the grid-aligned model for second-order computations of subsonic airfoil flows such as this.

Subsonic Separated Viscous Flow over an Airfoil

A practical case where an advantage of the grid-independent model over the grid-aligned model *is* fully realized in a second-order computation is for viscous separated flow over a NACA 0012 airfoil at $M = 0.5$, $\alpha = 3°$, and $\mathrm{Re} = 5000$. Full Navier–Stokes computations are performed on a 257×97 C-mesh with outer boundary extent of 14 chords

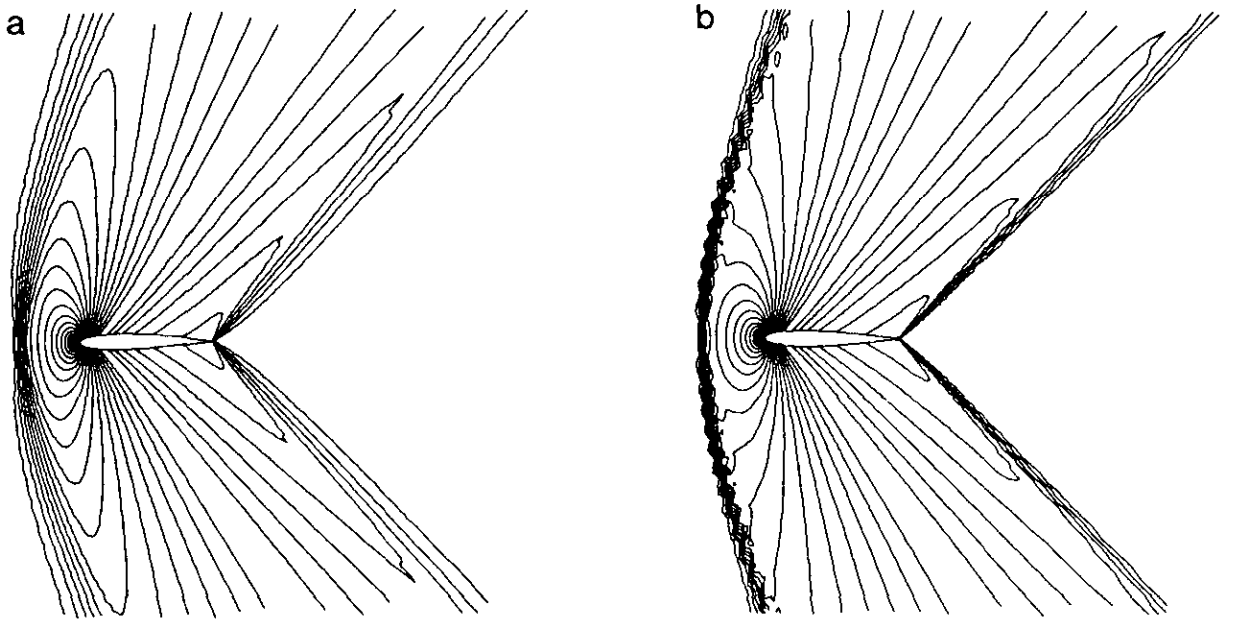

FIG. 10. Pressure contours for supersonic flow over NACA 0012 airfoil, first-order, 257×73 grid: (a) grid-aligned; (b) grid-independent.

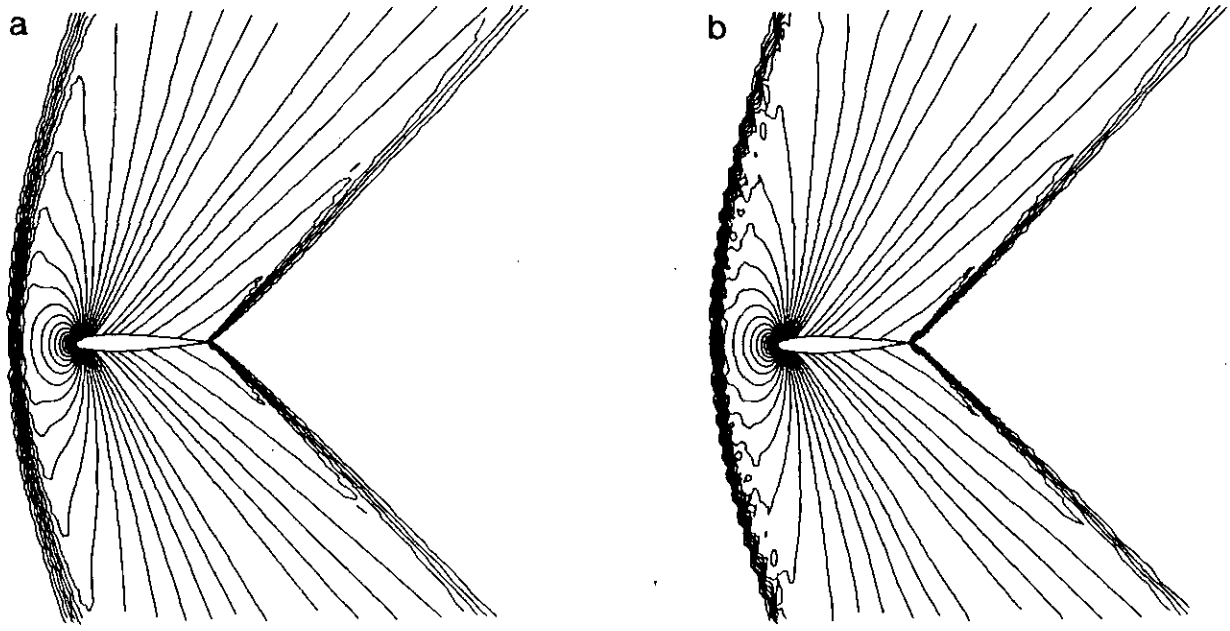

FIG. 11. Pressure contours for supersonic flow over NACA 0012 airfoil, second-order, 257 × 73 grid: (a) grid-aligned; (b) grid-independent.

and average minimum spacing on the body of 2×10^{-4} chords. There are 176 cell faces on the airfoil.

This test case was first discussed by Venkatakrishnan [17]. He found that on even reasonably fine meshes, the grid-aligned upwind scheme can produce erroneous results since there is a detached shear layer emanating from about midchord on the airfoil upper surface which is not oriented with the grid. The shear is misinterpreted by the grid-aligned model as a combination of shear and compression/expansion, with the end result of a distortion in the computed pressure. As the grid is refined, the distortion diminishes in magnitude. However, even on a mesh as fine as the 257×97, the computed pressure distortion is still clearly evident, as shown in Fig. 15a in a plot of pressure contours taken at intervals of 0.005. The grid-independent model result, given in Fig. 15b, essentially eliminates this distortion.

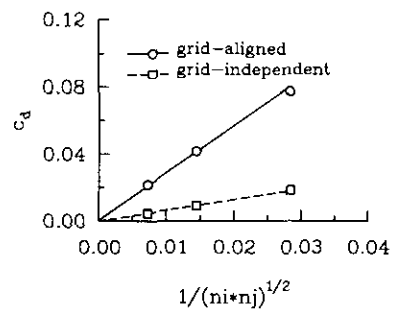

FIG. 12. Grid-convergence study for subsonic flow over NACA 0012 airfoil, first-order.

3D Oblique Supersonic Shear

A three-dimensional oblique supersonic shear case is computed within a cube 1.8 units on a side using a Cartesian $17 \times 17 \times 17$ mesh. The velocity undergoes both an increase in magnitude as well as a rotation through the shear layer. The shear layer itself is assumed to lie along one diagonal of the cube. Below the layer the nondimensional velocity components are $u = 3$, $v = 3$, and $w = 3$, while above the layer they are $u = 4$, $v = 2$, and $w = 4$. There is one transition cell where $u = 3.5$, $v = 2.5$, and $w = 3.5$. There is no pressure or density change across the shear layer.

A first-order computation using the grid-aligned model gives the in-plane Mach contour levels in Fig. 16, shown in increments of 0.05, for three different cuts through the cube. The exact solution (which is the initial condition for the computation) would show very narrowly spaced contours along the diagonal in the $i =$ constant plane, horizontally in the $j =$ constant plane, and vertically in the $k =$ constant plane. The shear layer is seen to spread a significant amount through the domain in this computation. The grid-independent model gives the results shown in Fig. 17. The shear layer is now preserved with fewer interior points. Although not shown, the maximum computed deviation in the pressure field from the exact solution (of no pressure change at all through the shear layer) is about 23% using the grid-aligned model, while the grid-independent model solution has a maximum error of only about 5%.

In-plane Mach contours from a second-order computation using the grid-aligned model are given in Fig. 18, while second-order grid-independent model results are given in

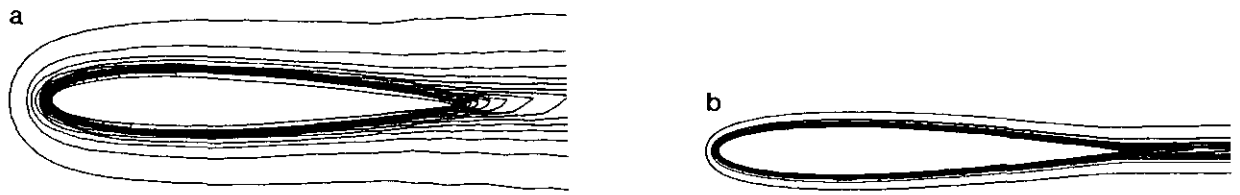

FIG. 13. Entropy contours for subsonic flow over NACA 0012 airfoil, first-order, grid-aligned: (a) 65×19 grid; (b) 257×73 grid.

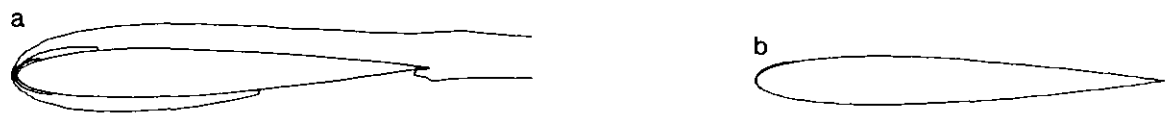

FIG. 14. Entropy contours for subsonic flow over NACA 0012 airfoil, first-order, grid-independent: (a) 65×19 grid; (b) 257×73 grid.

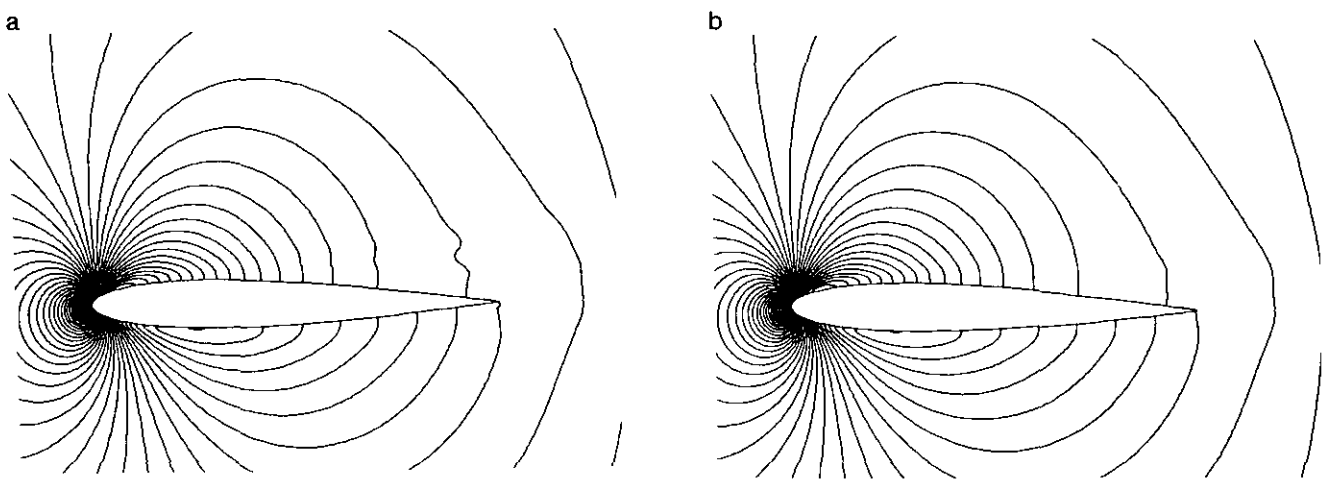

FIG. 15. Pressure contours for viscous flow over NACA 0012 airfoil, 257×97 grid: (a) grid-aligned; (b) grid-independent.

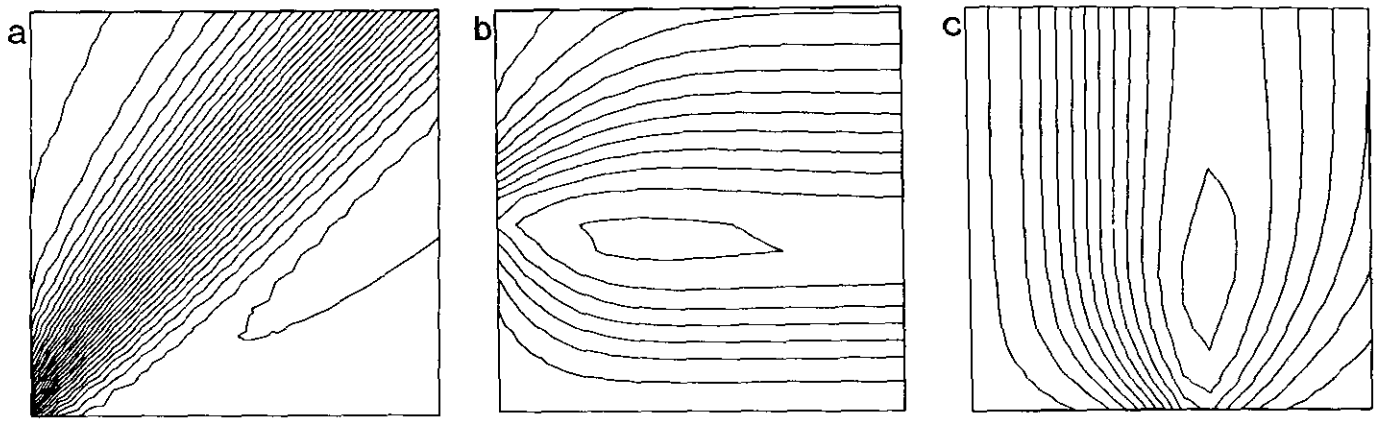

FIG. 16. In-plane Mach contours for 3D oblique shear, $17 \times 17 \times 17$ grid, first-order, grid-aligned: (a) $i = 9$ plane; (b) $j = 9$ plane; (c) $k = 9$ plane.

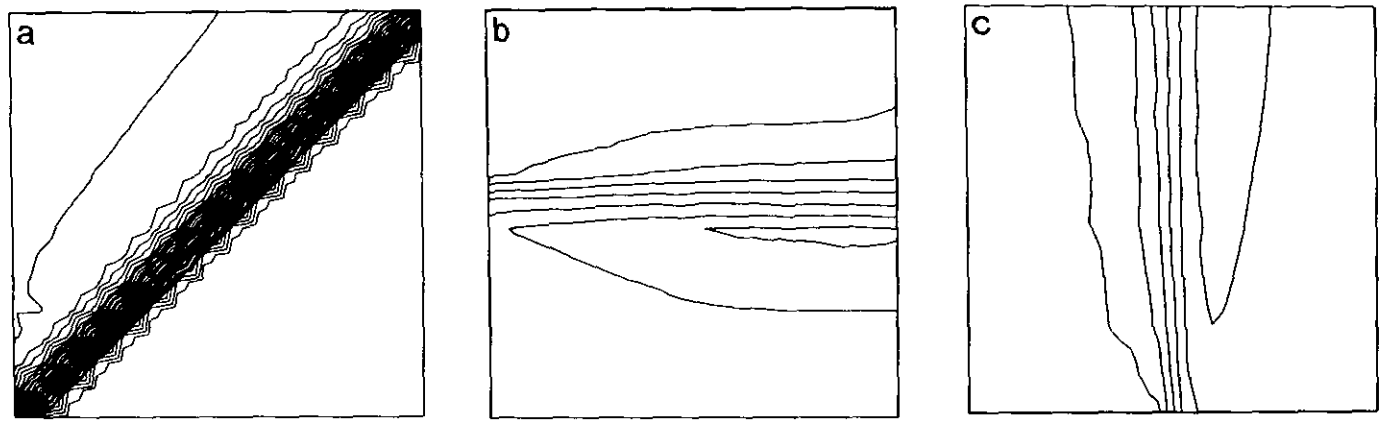

FIG. 17. In-plane Mach contours for 3D oblique shear, $17 \times 17 \times 17$ grid, first-order, grid-independent: (a) $i = 9$ plane; (b) $j = 9$ plane; (c) $k = 9$ plane.

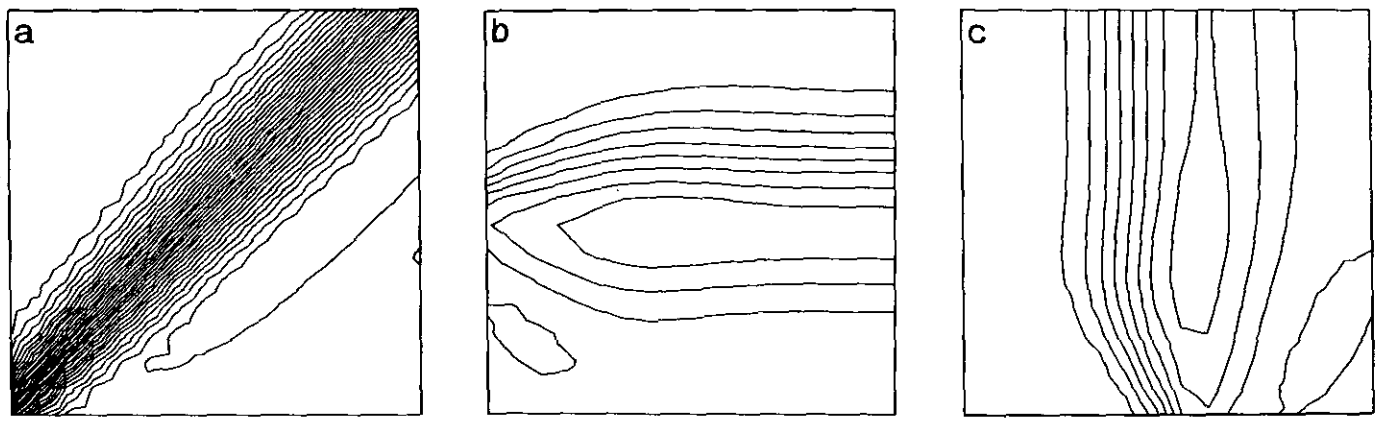

FIG. 18. In-plane Mach contours for 3D oblique shear, $17 \times 17 \times 17$ grid, second-order, grid-aligned: (a) $i = 9$ plane; (b) $j = 9$ plane; (c) $k = 9$ plane.

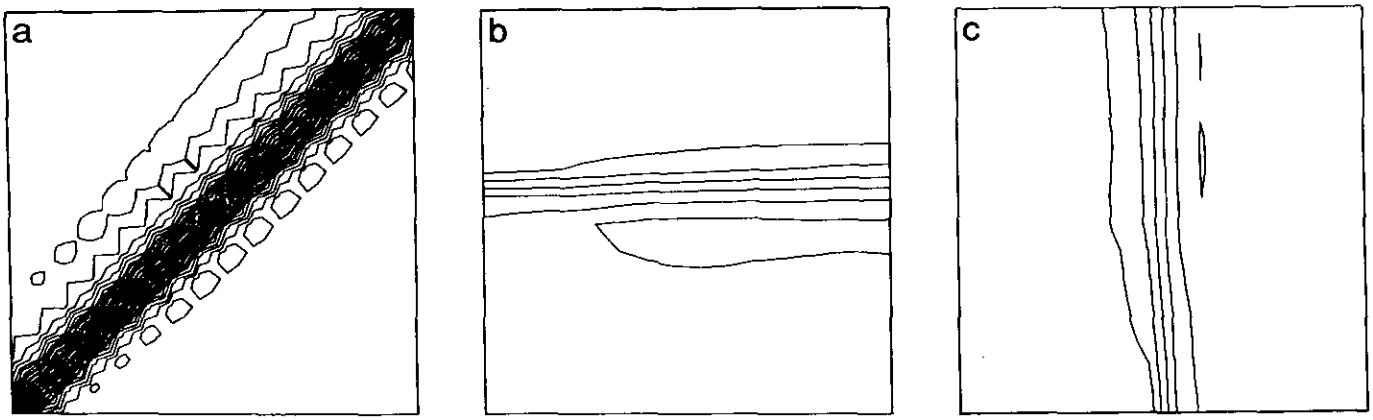

FIG. 19. In-plane Mach contours for 3D oblique shear, $17 \times 17 \times 17$ grid, second-order, grid-independent: (a) $i = 9$ plane; (b) $j = 9$ plane; (c) $k = 9$ plane.

Fig. 19. Even with second-order spatial accuracy the grid-independent model gives significantly higher shear-layer resolution than the grid-aligned model. The pressure field, not shown, is also computed more accurately. It has a maximum error of about 5%, while the grid-aligned result has a maximum error of about 10%.

4. CONCLUSIONS

Two-dimensional results obtained using the grid-independent model indicate that the method is generally worthwhile for first-order steady-state computations. Both an oblique shock reflection off a flat plate as well as supersonic flow over an airfoil with a detached bow shock and two trailing edge shocks that cut obliquely through the grid are computed more accurately using the grid-independent method than the grid-aligned method. Also, subsonic Euler airfoil-flow computations show significantly reduced entropy generation over the airfoil surface, resulting in better drag prediction. The grid-independent model is about 1.5 times more costly per iteration than the grid-aligned model and roughly 1.8 times as costly to reach the same level of convergence. Hence the cost penalty is not severe considering the increased accuracy of the first-order solutions.

When second-order spatial accuracy is employed, the small increase in accuracy attained by the grid-independent model is generally not worth the accompanying drawbacks. In particular, oblique shock waves are resolved only slightly more sharply than when using the grid-aligned method, and there is very little decrease in the numerical entropy generation for a subsonic airfoil computation. These facts, taken in combination with a propensity for increased oscillatory behavior near discontinuities, makes the grid-independent model an unattractive alternative to the grid-aligned model for second-order computations in general.

The only notable exceptions to this conclusion are found in cases involving oblique shear waves. Included in this category is the viscous flow over an airfoil for which the flow separates and a shear layer moves away from the body at an angle to the grid. In this case, numerical pressure oscillations evident in the separated region over the airfoil upper surface using the grid-aligned model are significantly reduced by the grid-independent model, which properly interprets the oblique waves present in the shear layer.

Conclusions from three-dimensional Euler test cases run along similar lines to those from two dimensions. For flows involving shock waves that lie oblique to the grid [14, 15], not shown in this paper, the grid-independent model improves the shock resolution considerably in a first-order computation, but second-order computations show very little difference from grid-aligned computations. An oblique supersonic shear wave, on the other hand, is resolved better using the grid-independent model for both first- and second-order computations.

Overall, then, for both two- and three-dimensional computations, the grid-independent model is seen to be worth the additional effort only for first-order spatially accurate computations, or computations involving only oblique shear waves. In general, inviscid flows with shock waves and/or flows with no shock or shear waves at all are better computed using the grid-aligned wave model when accuracy greater than first order is desired. The additional expense and oscillation-prone nature of the grid-independent model makes it unattractive for use in such cases.

Despite its shortcomings, the grid-independent model described in this paper can be thought of as a possible step in the right direction toward modeling the multidimensional flow physics of the Euler and Navier–Stokes equations more accurately than grid-aligned models. Its very low expense and modular nature (it is simply a flux function that can be inserted easily into an existing Euler or Navier–Stokes code) make it an attractive candidate for further analysis and development.

5. RELATED IDEAS AND FUTURE DIRECTIONS FOR MULTIDIMENSIONAL FLUX FUNCTIONS

Clearly, one of the primary drawbacks of the multidimensional flux function described in this paper is its propensity to generate spurious oscillations near computed shock and shear waves. Several ideas have been offered to improve the model's monotonicity properties. None have proved to be entirely satisfactory, although the angle-limiting procedure used for all results contained herein, which is based on a linearized monotonicity analysis, has given the best results for the widest range of test cases.

Another idea is described here because of its conceptual simplicity and potential for future improvement. The method consists of defining new left and right states at an interface that are more consistent with the locally assumed wave structure. An example of an assumed wave orientation is drawn in Fig. 20, for square cells. Here, assuming that constant states exist to the left and right of a wave at an interface, the shaded region represents the constant state $\mathbf{U}_L^*$ and the unshaded region represents the constant state $\mathbf{U}_R^*$. The average state in the left cell, however, is a combination of the states $\mathbf{U}_L^*$ and $\mathbf{U}_R^*$, area-weighted,

$$\mathbf{U}_L = \left(1 - \frac{a}{A}\right)\mathbf{U}_L^* + \frac{a}{A}\mathbf{U}_R^*, \tag{5.1}$$

where a is the area of the unshaded region in the left cell, and A is the area of the cell. A similar equation exists for $\mathbf{U}_R$. Solving for $\mathbf{U}_L^*$ and $\mathbf{U}_R^*$,

$$\begin{aligned} \mathbf{U}_L^* &= (1 + a^*)\,\mathbf{U}_L - a^*\mathbf{U}_R \\ \mathbf{U}_R^* &= (1 + a^*)\,\mathbf{U}_R - a^*\mathbf{U}_L, \end{aligned} \tag{5.2}$$

where

$$a^* \equiv \frac{(a/A)}{1 - 2(a/A)}. \tag{5.3}$$

When the wave angle (with respect to the grid face normal) is not zero, (5.2) has the effect of *increasing* the difference in states. This increases the numerical dissipation, which in turn may reduce the oscillatory nature of the solution.

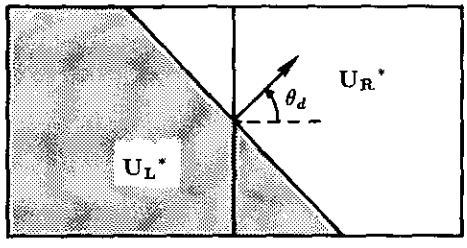

FIG. 20. Wave orientation in relation to Cartesian grid, showing left state $\mathbf{U}_L^*$ (shaded) and right state $\mathbf{U}_R^*$ (unshaded).

This method has the drawback that the computation of the area a becomes cumbersome for non-Cartesian grids. Additionally, it is unclear how to simultaneously redefine the left and right states for both θ_d waves *and* the $(\theta_d + \pi/2)$ shear wave while still maintaining the identity (2.14). However, when the left and right states are redefined based solely on the primary wave-propagation direction θ_d, preliminary computations on a Cartesian grid indicate that spurious oscillations can be reduced in magnitude using this method.

The current research has intentionally begun with the assumption that only the left and right states at each interface, obtained by interpolation along grid lines, are known at the beginning of the flux function computation. It is then up to the model to make the most of these input states and to infer from them the types and directions of waves likely to be present. This assumption was made to keep the cost of the grid-independent flux function as low as possible. By ignoring other surrounding flowfield data, no complex interpolations are required to obtain gradients in non-grid-oriented directions. However, practical experience indicates that this initial assumption may adversely effect the numerical solution. The inclusion of multidimensional input states might be helpful or even necessary to improve the robustness of the model, particularly in regard to monotonicity.

Some evidence in support of this idea comes from Parpia [7], who has developed an unstructured finite-volume Euler algorithm with a flux function similar to the one described in this paper. However, wavestrengths and orientations are now determined from gradients within each triangular cell rather than from data along a line. The incorporation of this extra information into the flux function appears to improve the quality of the solutions by reducing many of the spurious oscillations without resorting to any type of angle-limiting procedure. Additionally, results can now be converged several orders of magnitude without tricks such as freezing wave-propagation directions. Since this and other related research [16] are still evolving rapidly, however, it is difficult to draw any firm conclusions regarding the necessity of including multidimensional data in order to improve the robustness and monotonicity of these models. Certainly the cost and complexity must always be weighed against the solution quality in order for any method to become practical for general use.

REFERENCES

1. A. Dadone and B. Grossman, AIAA Paper 91-0635, 1991 (unpublished).
2. S. Davis, *J. Comput. Phys.* **56**, 65 (1984).
3. S. Godunov, *Math. Sb.* **47**, 271 (1959).

4. C. Lacor and C. Hirsch, *AIAA J.* **30**, 56 (1992).
5. D. Levy, K. Powell, and B. van Leer, AIAA Paper 89-1931-CP, 1989 (unpublished).
6. S. Obayashi and P. Goorjian, AIAA Paper 89-1957-CP, 1989 (unpublished).
7. I. Parpia, private communication (1991).
8. I. Parpia and D. Michalek, AIAA Paper 90-3016-CP, 1990 (unpublished).
9. I. Parpia and D. Michalek, AIAA Paper 91-1545-CP, 1991 (unpublished).
10. K. Powell and B. van Leer, AIAA Paper 89-0095, 1989 (unpublished).
11. P. Roe, *J. Comput. Phys.* **43**, 357 (1981).
12. P. Roe, *J. Comput. Phys.* **63**, 458 (1986).
13. C. Rumsey, B. van Leer, and P. Roe, AIAA Paper 91-1530-CP, 1991 (unpublished).
15. C. Rumsey, Ph.D. thesis, University of Michigan, 1991 (unpublished).
16. R. Struijs, H. Deconinck, P. DePalma, P. Roe, and K. Powell, AIAA Paper 91-1550, 1991 (unpublished).
17. V. Venkatakrishnan, *Comput. Fluids* **18**, 191 (1990).